Large-Area Electron Beam Melting: Frequency Analysis and Critical Frequency Prediction

Brodan Richter
Department of Mechanical Engineering,
University of Wisconsin–Madison,
Madison, WI 53706

Frank E. Pfefferkorn[1]
Department of Mechanical Engineering,
University of Wisconsin–Madison,
Madison, WI 53706
e-mail: frank.pfefferkorn@wisc.edu

During large-area electron beam irradiation, high energy flux pulses of electrons melt a thin layer of material. The objective of this work is to analyze the spatial frequencies of a turned, S7 tool steel surface before and after electron beam melting. It was observed that high frequency features are significantly reduced following melting, but lower frequency features were created and increased the unfiltered areal average roughness. Previous work on laser remelting-based polishing derived a critical frequency that defines the frequency above which higher frequency features are dampened. As the critical frequency depends on the melt duration that the surface experiences, a one-dimensional, transient temperature prediction model was created for this work to estimate the melt time for a single electron beam pulse. This model allowed for the calculation of a critical frequency that showed good ability to predict the frequencies that are dampened.
[DOI: 10.1115/1.4043236]

Keywords: electron beam melting, polishing, critical frequency, tool steel

1 Introduction

In large-area electron beam irradiation, a plasma source creates a plasma cloud between the cathode and collector. After the cloud is formed, the cathode has an accelerating voltage applied to it that causes an electron beam to form. This electron beam delivers a highly concentrated energy flux that rapidly melts metallic surfaces [1]. Large-area electron beam melting has previously been shown to reduce the roughness from approximately 6 μm to 0.7 μm R_z and increase the glossiness on NAK80 mold steel surfaces [2]. Additionally, the irradiated surfaces were found to better resist corrosion compared to a nonirradiated surface. Improvements in roughness were also observed with incident angles from 0 to 60 deg making it a valuable process for metal mold finishing. The process has also been demonstrated to work for finishing intricate AISI 630 steel molds containing various microcircular and square rods and holes [3]. The roughness of the substrate was also reduced from 149.8 nm to 26.72 nm R_a. Other work studied temperature prediction during the process with a three-dimensional, transient simulation for four different metallic alloys [4]. That work modeled the electron beam absorption by a volumetric generation method that was also utilized in this work. The predictions from that simulation were shown to give good agreement with the melt depths observed after sectioning irradiated samples.

Laser melting is a similar process to electron beam irradiation that has also found use in smoothing surfaces [5]. By assuming that surface features on a molten surface, following irradiation, can be modeled as surface capillary waves, a critical frequency was derived that predicts the frequency above which features are significantly dampened [6]. That critical frequency was later used to create a surface prediction model for capillary regime laser polishing that uses a low-pass Gaussian spatial filter with the break feature at the critical frequency [7]. In this work, a rough surface and a smooth-turned surface are studied before and after large-area electron beam irradiation. In contrast to previous work on electron beam irradiation, the surface analysis in this work focuses on microscale metrology measurements and the examination of the power spectrum of the initial and electron beam melted surfaces. Additionally, this work uses a temperature prediction model to estimate the melt duration and corresponding critical frequency for the irradiated surfaces to study if it is applicable to electron beam irradiated surfaces in addition to laser melted surfaces.

2 Methods

2.1 Material Preparation and Surface Analysis. Fifteen 31.75 mm-diameter, 7 mm-thick samples were turned from AISI S7 round stock at 1000 rpm and constant feed of 0.05 mm/rev on a mill turn center (Mori Seiki, NT1000, Nagoya, Japan). The two samples with the highest and lowest roughness were used in this study to characterize the effect of large-area electron beam irradiation on surfaces with similar surface frequency components of different amplitudes. The nominal chemical composition of AISI S7 tool steel is given in Table 1, and the material properties used in the temperature prediction model in Sec. 2.2 are given in Table 2.

The samples were cleaned after machining and before imaging with methanol and delicate task wipes. Measurements of the surfaces were made before and after electron beam irradiation using a white light interferometer (Zygo NewView 6300, Middlefield, CT) with a 20× objective, lateral resolution of 0.87 μm, and instrument vertical resolution of up to 0.1 nm. The measurements were made at nine evenly spaced locations between 2 mm and 10 mm from the center of the sample, and the results presented in Sec. 3.2 are an average of those nine measurements. Unfiltered and waviness-filtered areal average roughnesses (S_a) are calculated in accordance with ASME B46.1-2009. The waviness is filtered out using a Gaussian filter with a cutoff wavelength of 80 μm.

2.2 Temperature Prediction Model. A one-dimensional, transient, finite difference thermal model was developed to estimate melt duration during each pulse of the electron beam. The governing equation was solved with a variable-step, variable-order, implicit technique and it is given in the below equation:

$$\frac{\partial T(z,t)}{\partial t} = \frac{k}{\rho\, c(T)} \frac{\partial^2 T(z,t)}{\partial z^2} + \frac{\dot{g}(z,t)}{\rho\, c(T)} \tag{1}$$

where T is the temperature, t is the time, k is the thermal conductivity, z is the positon, $\dot{g}$ is the node-specific thermal generation term, ρ is th density, and c is the specific heat. The temporal and spatial boundary conditions used are given in below equations:

Table 1 Nominal S7 tool steel composition [8]

C	Mn	Si	Cr	Fe
0.45–0.55	0.2–0.9	0.2–1.0	3.0–3.5	Balance
Mo	**V**	**P**	**S**	
1.3–1.8	<0.35	<0.03	<0.03	

[1]Corresponding author.

Contributed by the Manufacturing Engineering Division of ASME for publication in the Journal of Micro- and Nano-Manufacturing. Manuscript received November 2, 2018; final manuscript received March 2, 2019; published online April 11, 2019. Assoc. Editor: Irene Fassi.

Table 2 Material properties

Density, ρ [9]	kg/m^3	7800
Thermal conductivity, k [9]	W/m K	28.9
Specific heat capacity, c [9]	J/kg K	460
Thermal diffusivity, α	mm^2/s	8.055
Viscosity (iron) μ [10]	mPa·s	5.5
Initial temperature, T_0	K	293
Surroundings temperature, T_{surr}	K	293
Solidus temperature [11]	K	1618
Liquidus temperature [11]	K	1733
Enthalpy of fusion [11]	kJ/kg	245.3
Boiling temperature (iron) [12]	K	3273
Enthalpy of vaporization (iron) [12]	kJ/kg	6339
Emissivity, ε [13]	—	0.69

$$\sigma\,\varepsilon\left(T_{surr}^4 - T(z=0,t)^4\right) = -k\frac{\partial T(z=0,\,t)}{\partial z} \tag{2}$$

$$T(z = L_{sim}, t) = T_0 \tag{3}$$

$$T(z, 0) = T_0 \tag{4}$$

where σ is the Stefan–Boltzmann constant, ε is the emissivity of the surface, T_{surr} is the temperature of the surroundings, and T_0 is the initial temperature. The model simulates the energy absorption from the electron beam through a volumetric generation term calculated by the fractional absorption of transmitted electrons [4]. A probability density function of the electron absorption is shown in Fig. 1.

The area under the plot represents the total absorption verses depth and indicates that almost all of the absorption of the electron beam occurs within the first two micrometers of material. The enthalpy of fusion and vaporization was considered in the model through the apparent heat capacity method [14]. To use the apparent heat capacity to simulate boiling, it was assumed that boiling begins 30 K below the actual boiling temperature. The depth of the simulated sample was chosen to be five times the thermal penetration depth associated with the simulation time and the duration of the simulation was chosen to be long enough for the surface to resolidify. The simulation parameters are given in Table 3.

2.3 Electron Beam Melting (Polishing). Large-area electron beam irradiation was performed with an electron beam finish machine (Sodick EBMPF32A, Yokohama, Japan). The process was performed at a vacuum pressure of 0.05 Pa and with argon as an inert gas in the irradiation chamber. The samples were stationary during the irradiation process. The irradiation parameters used for the samples of this study are given in Table 4. They were chosen based on preliminary experiments on the turned samples with intermediate roughness.

2.4 Critical Frequency Prediction. The critical frequency, which is the frequency above which surface features are

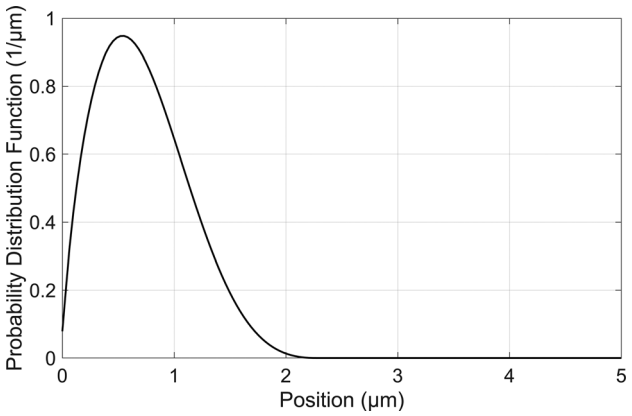

Fig. 1 Probability distribution function of electron beam absorption

Table 3 Temperature prediction model properties

Number of time steps	—	29,981
Total simulation duration	μs	15
Number of position nodes	—	3001
Nodal spacing	nm	32.5
Total simulation length	μm	97.4

significantly dampened, has been derived from surface capillary wave dispersion relations as [6]

$$f_{cr} = \sqrt{\frac{\rho}{\pi^2 \mu\, t_{melt}}} \tag{5}$$

where $f_{cr,individual}$ is the critical frequency, ρ is the density, μ is the viscosity, and t_{melt} is the melt duration. In this work, as the surface is exposed to ten 2 μs pulses with between 10 s and 15 s between pulses, it is expected that the surface fully cools back to the initial temperature between each individual pulse. This necessitates an expression for the critical frequency of a sequence of independent melt events. It is assumed that the melt duration of Eq. (5) can be multiplied by the total number of melt events (N_{melt} events, i.e., number of pulses) to give the total critical frequency. This is shown in below equation:

$$f_{cr,\,total} \approx \sqrt{\frac{\rho}{\pi^2 \mu\,(t_{melt} * N_{melt}\ \text{events})}} = \frac{f_{cr}}{\sqrt{N_{melt}\ \text{events}}} \tag{6}$$

The melt duration is determined with the temperature prediction model presented in Sec. 2.2. However, due to the mushy zone, two different melt durations are defined: $t_{melt,max}$, which is the time period between the surfaces initially crossing the solidus temperature and later falling back below the solidus temperature and $t_{melt,min}$, which is similar but instead uses the liquidus temperature.

3 Results

3.1 Temperature Prediction. Results at various depths from the temperature prediction model are shown in Fig. 2.

It can be seen that the surface of the material reaches the boiling temperature within the 2 μs electron beam pulse but does not go over due to the enthalpy of vaporization. However, as the simulation uses a finite node size, localized ablation on the surface may occur. Additionally, due to the volumetric absorption of the electron beam, the highest temperature occurs at a distance 0.357 μm into the material. The melt duration for the surface and the corresponding critical frequency are given in Table 5.

3.2 Electron Beam Polishing. The measured surface before and after large-area electron beam irradiation is shown in Fig. 3. The machining marks are visible in the as-machined surface causing a highly anisotropic surface with strong surface texture directionality. After irradiation, the machining marks are no longer visible but instead larger wavelength surface features are

Table 4 Electron beam irradiation parameters

Pulse duration	μs	2
Number of pulses	—	10
Time between pulses	s	10–15
Cathode voltage	kV	25
Solenoid voltage	kV	1.5
Chamber pressure	Pa	0.05
Beam radius	mm	30
Energy density	J/cm^2	7
Power density	kW/mm^2	35
Sample processing time	min	11

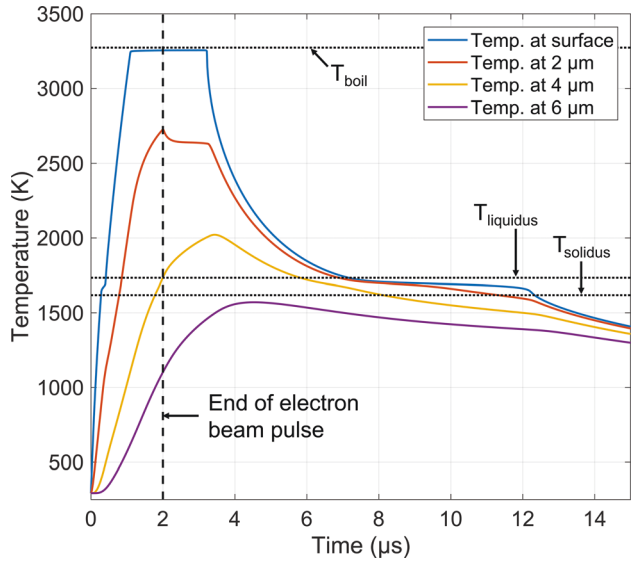

Fig. 2 Temperature of the sample at various depths

Table 5 Predicted melt durations and corresponding critical frequencies

		$T_{melt} = T_{solidus}$	$T_{melt} = T_{liquidus}$
t_{melt}	μs	12.05	6.75
$f_{critical}$	mm^{-1}	12.21	16.31

observed. The surface also appears to be more isotropic than before. The areal average roughness of the original and waviness-filtered surfaces is given in Table 6.

The roughness of the unfiltered surface increased following electron beam irradiation. However, as the filtered values show, the roughness is primarily due to the large wavelength features that have been created by the surface melting process and are visible in Fig. 3. The unfiltered roughness of the rougher sample after electron beam melting is higher than that of the smoother sample, but the filtered roughnesses of both of them are approximately the same. Power spectrum plots for the *Y*-direction and *X*-direction are given in Figs. 4 and 5, respectively.

The power spectrum plots agree with the unfiltered and filtered areal average roughness results. The electron beam remelted samples show higher amplitudes at the lower frequency values, but lower amplitudes at higher frequency values. The power spectrum plots also indicate that the frequencies of both the rougher and smoother samples are very similar to each other between 0.01 μm^{-1} and 0.05 μm^{-1} in both the *X*- and *Y*-directions. The

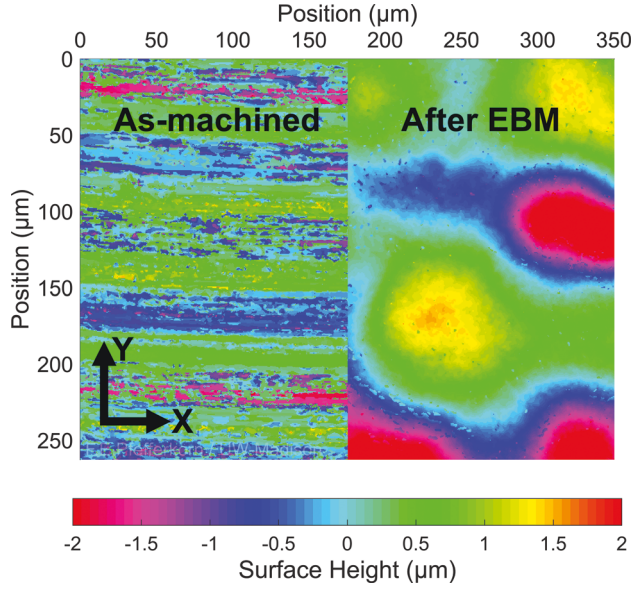

Fig. 3 Measured surface topography (*a*) before and (*b*) after electron beam polishing

Table 6 Roughness of the unpolished and polished surfaces (values after ± are standard deviation)

Sample	S_a (μm)	Filtered S_a (μm)
Rougher surface		
As-machined	0.53 ± 0.10	0.46 ± 0.09
After EBM	0.81 ± 0.16	0.25 ± 0.04
Smoother surface		
As-machined	0.23 ± 0.02	0.21 ± 0.02
After EBM	0.66 ± 0.16	0.21 ± 0.03

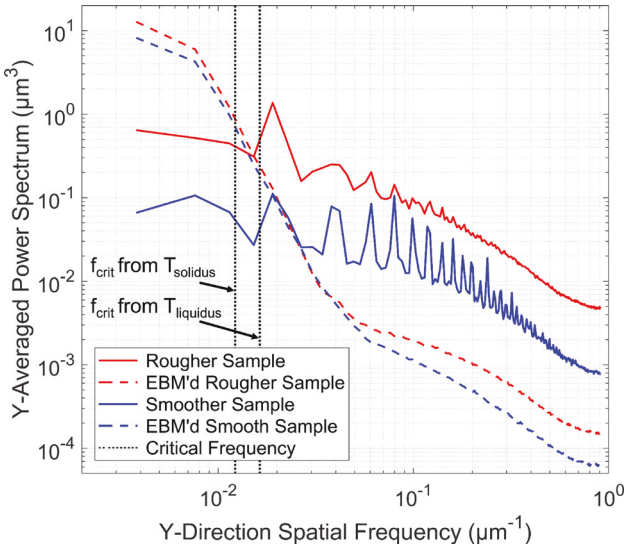

Fig. 4 Power spectrum of frequencies in the *Y*-direction

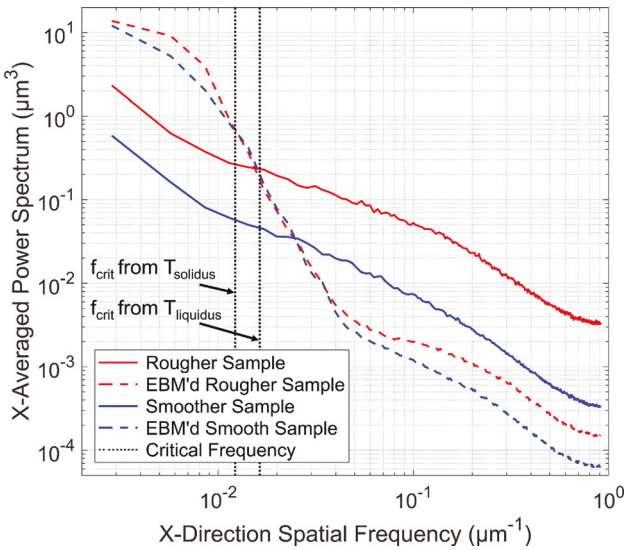

Fig. 5 Power spectrum of frequencies in the *X*-direction

X-and *Y*-direction frequencies are also very similar to each other following polishing, which supports the previous observation in Fig. 3 about a more isotropic irradiated surface. The critical frequency predicted by the temperature prediction model appears to give a good approximation of the frequencies that will get reduced during electron beam polishing.

The reason for the increase in low frequency features is not clear. It may be due to the temperature at the surface reaching the boiling temperature, causing localized areas of ablation that may have induced the new surface features. Alternatively, since the electron beam is absorbed volumetrically and the hottest region was found to be 0.357 μm within the material, material below the surface may have begun to vaporize causing upwards bulging. An additional potential reason is that the carbides within the S7 tool steel may have caused localized temperature variations and the creation of additional low frequency features.

4 Conclusions

In this work, the surfaces of two S7 tool steel samples that have been turned are studied before and after large-area electron beam melting. This work demonstrates that electron beam melting strongly reduces higher spatial frequency features but may induce lower frequency features that increase the overall roughness in certain ferrous alloys. The power spectrum presented for these surfaces before and after electron beam melting also gives insight on the frequencies of a surface after the process. This information informs on tribological properties such as on how these surfaces perform in wear, adhesion, and frictional tests. Additionally, this work shows that the critical frequency previously used in the prediction of dampened frequencies for laser polishing can be applied to electron beam melting if the melt duration is known. This ability to predict the frequencies that are dampened allows users of the large-area electron beam melting process better assessment of whether the process can effectively smooth the surfaces they are interested in.

Acknowledgment

The authors would like to thank Sodick Co., Ltd. for performing the electron beam melting tests for this work. Additionally, this work used NSF-supported shared facilities at the University of Wisconsin–Madison.

Funding Data

- The U.S. National Science Foundation (NSF) (Grant No. CMMI-1727366; Funder ID: 10.13039/501100008982).

References

[1] Proskurovsky, D. I., Rotshtein, V. P., Ozur, G. E., Markov, A. B., Nazarov, D. S., Shulov, V. A., Ivanov, Y. F., and Buchheit, R. G., 1998, "Pulsed Electron-Beam Technology for Surface Modification of Metallic Materials," J. Vac. Sci. Technol. A, **16**(4), pp. 2480–2488.

[2] Uno, Y., 2007, "A New Polishing Method of Metal Mold With Large-Area Electron Beam Irradiation," J. Mater. Process. Tech., **187–188**, pp. 77–80.

[3] Murray, J. W., Kinnell, P. K., Cannon, A. H., Bailey, B., and Clare, A. T., 2013, "Surface Finishing of Intricate Metal Mould Structures by Large-Area Electron Beam Irradiation," Precis. Eng., **37**(2), pp. 443–450.

[4] Kim, J., Lee, W. J., and Park, H. W., 2018, "Temperature Predictive Model of the Large Pulsed Electron Beam (LPEB) Irradiation on Engineering Alloys," Appl. Therm. Eng., **128**, pp. 151–158.

[5] Bordatchev, E. V., Hafiz, A. M. K., and Tutunea-Fatan, O. R., 2014, "Performance of Laser Polishing in Finishing of Metallic Surfaces," Int. J. Adv. Manuf. Tech., **73**(1–4), pp. 35–52.

[6] Perry, T. L., Werschmoeller, D., Duffie, N. A., Li, X., and Pfefferkorn, F. E., 2009, "Examination of Selective Pulsed Laser Micropolishing on Microfabricated Nickel Samples Using Spatial Frequency Analysis," ASME J. Manuf. Sci. Eng., **131**(2), p. 021002.

[7] Vadali, M., Ma, C., Duffie, N. A., Li, X., and Pfefferkorn, F. E., 2012, "Pulsed Laser Micro Polishing: Surface Prediction Model," J. Manuf. Process., **14**(3), pp. 307–315.

[8] ASTM International, 2015, "Standard Specification for Tool Steels Alloy," ASTM International, West Conshohocken, PA, Standard No. ASTM A681-08 2015.

[9] MatWeb, 2019, "Bohler-Uddeholm COMPAX™ AISI S7 MOLD QUALITY Cold Work Steel," MatWeb, accessed Mar. 26, 2019, http://www.matweb.com/search/datasheet.aspx?matguid=41a925eea26a46b6b8528ef80c68a992

[10] Battezzati, L., and Greer, A. L., 1989, "The Viscosity of Liquid Metals and Alloys," Acta Metall. Mater., **37**(7), pp. 1791–1802.

[11] Kalup, A., Smetana, B., Kawuloková, M., Zlá, S., Francová, H., Dostál, P., Waloszková, K., Waloszková, L., and Dobrovská, J., 2017, "Liquidus and Solidus Temperatures and Latent Heats of Melting of Steels," J. Therm. Anal. Calorim., **127**(1), pp. 123–128.

[12] Zhang, Y., Evans, J. R. G., and Yang, S., 2011, "Corrected Values for Boiling Points and Enthalpies of Vaporization of Elements in Handbooks," J. Chem. Eng. Data, **56**(2), pp. 328–337.

[13] Saqid, H., 2012, "Determination of Steel Emissivity for the Temperature Prediction of Structural Steel Members in Fire," J. Mater. Civ. Eng., **25**(2), pp. 167–173.

[14] Hu, H., and Argyropoulos, S. A., 1996, "Mathematical Modelling of Solidification and Melting: A Review," Model. Simul. Mater. Sci. Eng., **4**(4), pp. 371–396.